A Broadband Free-Space Millimeter-Wave Vector Transmission Measurement System

Yoshiyuki Konishi, Masayuki Kamegawa, Michael Case, Ruai Yu, Scott T. Allen, and Mark J. W. Rodwell

Abstract— **We report both broadband monolithic transmitter and receiver IC's for mm-wave electromagnetic measurements. The IC's use a nonlinear transmission line (NLTL) and a sampling circuit as a picosecond pulse generator and detector. The pulses are radiated and received by planar monolithic bowtie antennas, collimated with silicon substrate lenses and off-axis parabolic reflectors. Through Fourier transformation of the received pulse, accurate 30–250 GHz free space gain-frequency and phase-frequency measurements are demonstrated. Systems design considerations are discussed, and a variety of mm-wave broadband transmission measurements are demonstrated.**

I. Introduction

FOR mm-wave gain-frequency measurement systems, convenient and broadband sources and detectors have been required for some time. Measurement systems based on waveguide components [1] have played a dominant role, but each component has narrowband frequency coverage (1.5:1). To measure over a broad bandwidth, many waveguide systems must be used, which is both inconvenient and expensive. Additionally, >100 GHz waveguides are difficult to machine and require precise assembly.

Another submillimeter-wave measurement technique uses antenna-coupled photoconductors to radiate and detect subpicosecond electromagnetic pulses. The photoconductors are excited by lasers having subpicosecond pulse durations. Through Fourier analysis of the received pulse, the amplitude and phase transmission functions of materials can be measured at frequencies as high as ~3 THz [2]. The primary difficulty is in the size and cost of the apparatus.

The mm-wave measurement system reported here [3] radiates and detects picosecond pulses and obtains frequency information through Fourier transformation. The system uses solid-state monolithic devices, a nonlinear transmission line (NLTL) for pulse generation and a sampling circuit for signal detection [3]-[6]. The NLTL-based system is much more compact than laser systems, and has a frequency resolution determined by the phase noise and frequency resolution of the microwave drive sources employed. Because the NLTL input frequency can be varied by as much as one octave, the system can easily be tuned to a desired mm-wave harmonic frequency. Compared to waveguide-based systems, the NLTL-based system covers a 30–250 GHz bandwidth with a single experimental setup, and a set of mm-waveguide components are replaced by a pair of GaAs IC's.

Manuscript received May 19, 1993; revised September 14, 1993. This work was supported in part by the Air Force Office of Scientific Research under Grant F49620-92-J-0469 and under an associated AFOSR/AASERT grant F49620-92-J-0365.

The authors are with the Department of Electrical and Computer Engineering, University of California, Santa Barbara, CA 93106 USA.

IEEE Log Number 9402379.

II. The Transmitter and Receiver

NLTL's and NLTL-gated sampling circuits permit generation and detection of transient signals with ~1 ps risetimes. A circuit diagram of the NLTL is shown in Fig. 1(a); a detailed discussion of their design and operation is given in [5]. In the NLTL, a high-impedance transmission line with characteristic impedance Z_1 is periodically loaded, at spacings τ (in units of time) by Schottky varactor diodes, producing a synthetic transmission line whose propagation velocity is voltage-dependent. As a negative-going input voltage transition (either a step-function or the negative-going transitions of a sinusoidal input signal) with initial voltage v_l, final voltage v_h and falltime $T_{f,\text{in}}$ propagates along the line, the fall time will at first decrease linearly with propagation distance due to the differential propagation delay $\Delta T = T(v_h) - T(v_l)$ along the wavefront, where $T(v) = n\sqrt{LC_T(v)}$. $L = Z_1\tau$ is the inductance per line section, n is the number of diodes past which the signal has propagated, $C_T(v) = C_j(v) + \tau/Z_1$ is the total capacitance per line section and $C_j(v)$ is the voltage-variable diode junction capacitance. As the fall time decreases, dispersion arising from the periodic-line cutoff frequency, $\omega_{\text{per}} \simeq 2/\sqrt{LC_{ls}}$, and the varactor cutoff frequency, $\omega_{d,ls} = 1/r_s C_{ls}$, competes with the compression arising from the voltage-dependent propagation velocity. Here $C_{ls} = (Q(v_h) - V(v_l))/(v_h - v_l)$ is the varactor large-signal (average) capacitance and r_s is the diode series resistance. A final limited falltime $T_{f,\min}$ is reached at which the falltime compression per section arising from ΔT is balanced by the falltime broadening per section arising from ω_{per} and $\omega_{d,ls}$. If the diode cutoff frequency dominates, $T_{f,\min} \propto 1/\omega_{d,ls}$, and wavefront transition times of ~1–2 ps are feasible given diodes with cutoff frequencies of 1–2 THz. With a sinusoidal input signal, the NLTL forms shock-waves from the negative-going half-cycles of the sinusoid, producing a sawtooth output waveform with significant power at high-order harmonics of the signal frequency.

A 2-diode-bridge sampling circuit (Fig. 1(b)) measures the received signal. As with the NLTL, a detailed circuit description is given in [5]. A second NLTL, also driven by a 7–14 GHz microwave synthesizer, generates a sawtooth waveform with 1.5 ps falltime. The step-functions generated by this NLTL are converted into a pair of positive-going and negative-going impulses using a combined balun and

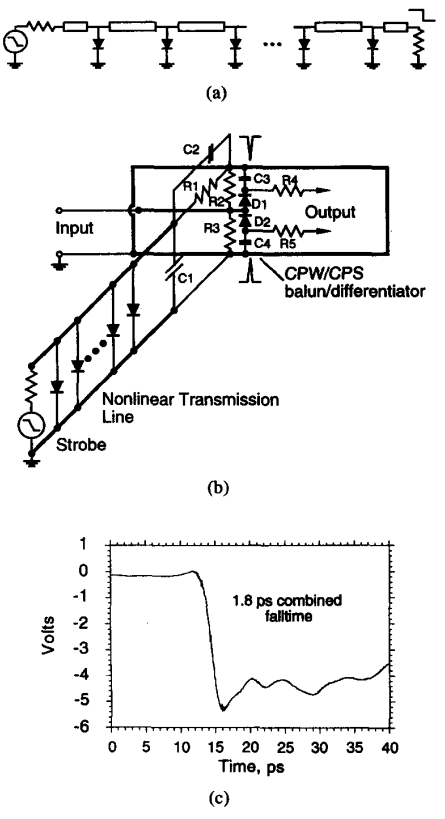

Fig. 1. NLTL (a) and sampling circuit (b) schematics, and (c) NLTL output measured by a sampling circuit.

differentiator network implemented in coplanar waveguide and coplanar strip transmission lines. The strobe NLTL is coupled to this balun/differentiator through a rudimentary impedance-matching network ($C1$, $C2$, and $R1$). A pair of sampling diodes ($D1$ and $D2$), normally held in reverse bias, are driven momentarily into forward conduction by the symmetric positive and negative impulses. During this period, the sampling aperture period, the diodes are in a low-impedance state and the input signal can partially charge a pair of hold capacitors ($C3$ and $C4$) placed in series with the two sampling diodes. If the strobe frequency is synchronous with the signal frequency, the circuit will repetitively sample the input signal at a fixed point within its repetition period, and the sampled output, coupled through resistors $R4$ and $R5$, will asymptotically charge to a voltage equal to the value of the input voltage waveform at the time of the strobe pulse. The full waveform of the input signal is measured by slowly varying the relative timing of the input and strobe signals, this being accomplished by offsetting the strobe frequency from the signal repetition frequency by approximately 100 Hz. Fig. 1(c) shows an NLTL output measured by an NLTL-gated sampling circuit. The measured 1.8 ps transition time is the convolution of the NLTL falltime and the sampling circuit risetime.

The free-space measurement system requires wideband on-wafer antennas. The bowtie antenna, linearly tapered coplanar strip (V) antenna, and linearly-tapered CPW antenna (slot-V) all are scale-invariant structures having frequency independent far-field radiation patterns and radiation impedances [8]-[10]. The bow-tie has a multi-lobed radiation pattern (resulting in spatial non-uniformity of the collimated beam) but permits close integration with the NLTL and with the sampling circuits. The recently-reported slot-V antenna [10] has a better-collimated radiation pattern, and would in fact be preferred over the bowtie for this application.

The transmitter NLTL is fabricated within one electrode plane of the bowtie antenna, and drives the 120° (52Ω impedance) antenna through a coplanar waveguide (CPW) feed network (Fig. 2(a)). Two 100Ω resistances at the antenna perimeter terminate the antenna at frequencies below the antenna low-frequency cut-off. The receiver is a bow-tie antenna interfaced through a similar antenna feed (Figs. 2(b) and 3). The 50Ω sampling circuit input impedance terminates the receiving antenna without reflection.

Metallic losses of traveling-wave antennas are small even at sub-mm-wave frequencies. To demonstrate this simply, we calculate the net skin loss on a tapered-coplanar-strip (V) antenna (Fig. 4(a)). In the limit of small angles θ_1 and θ_2, the skin and radiation losses of the V antenna can be computed from an integral with respect to distance of the skin and radiation loss relationships of an (untapered) CPS line [8], [11]. Losses computed for the V antenna then also apply to a pair of counter-propagating V antennas fed by a single CPW (Fig. 4(b)), a structure similar to the bowtie antenna (Fig. 4(c)).

The power P_l propagating on the V antenna varies according to $dP_l/dz = -2(\alpha_r(z) + \alpha_s(z))P_l(z)$, where $\alpha_r(z)$ and $\alpha_s(z)$ are the radiation and skin attenuation coefficients per unit distance at position z. The power radiated is

$$P_r = \int_{z_{\text{feed}}}^{z_{\text{end}}} 2\alpha_r(z)P_l(z)dz \tag{1}$$

Given small θ_1 and θ_2, $\alpha_r(z)$ and $\alpha_s(z)$ can be approximated from CPS skin-effect and radiation loss expressions, where $s(z) = \theta_1 z$ and $d(z) = \theta_2 z$. Radiation loss is [8]

$$\alpha_r(z) = (\pi/2)^5\sqrt{2}(3-\sqrt{8})\sqrt{\epsilon_r^3+\epsilon_r^2}(1-1/\epsilon_r)^2 \times d^2(z)f^3/c^3K(k)K(k') \tag{2}$$

where f is the frequency in Hz, $\epsilon_r = 13$ the substrate dielectric constant, c the speed of light, $k = s/d$, $(k')^2 = 1 - k^2$, and $K(k)$ is the complete elliptic integral of first order. Skin loss is [11]

$$\alpha_s(z) \simeq \frac{\sqrt{\pi f\mu/\sigma}}{4Z_0 d(z)K^2(k')(1-s^2/d^2)} \times \left[\frac{2d}{s}\left(\pi + \ln\left(\frac{4\pi s(1-s/d)}{t(1+s/d)}\right)\right) + 2\left(\pi + \ln\left(\frac{4\pi d(1-s/d)}{t(1+s/d)}\right)\right)\right] \tag{3}$$

where $2w = d - s$, σ is the metal (gold) conductivity, μ the permeability of vacuum, t the metal thickness, and $Z_0 = 377\Omega\sqrt{2/(1+\epsilon_r)}K(k')/K(k)$ the CPS (and antenna) characteristic impedance.

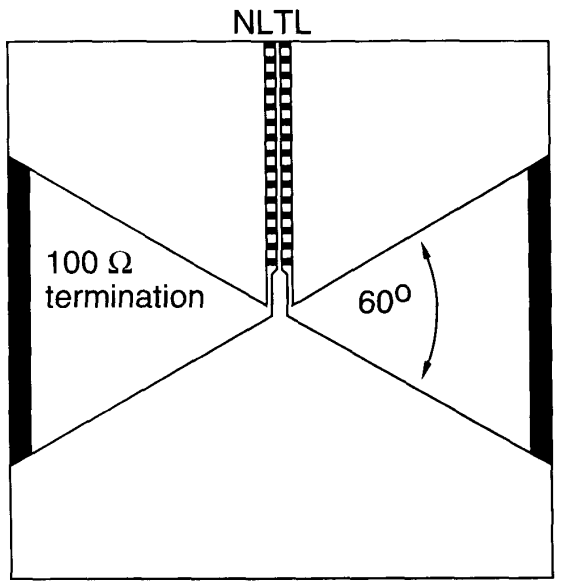

(a)

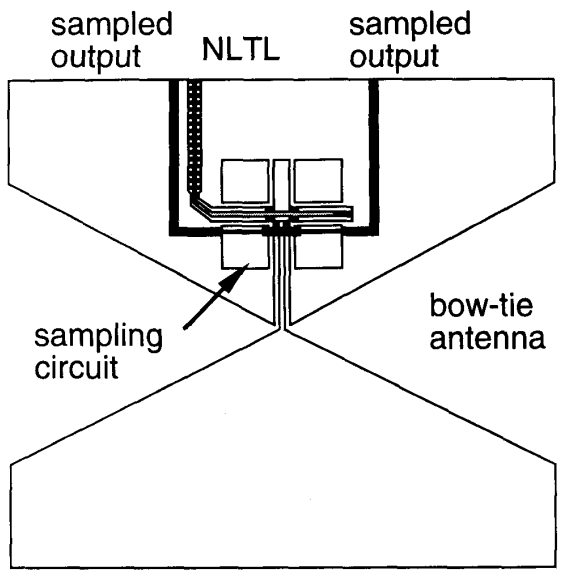

(b)

Fig. 2. Simplified approximate-scale integrated circuit layouts of (a) picosecond transmitter and (b) picosecond receiver.

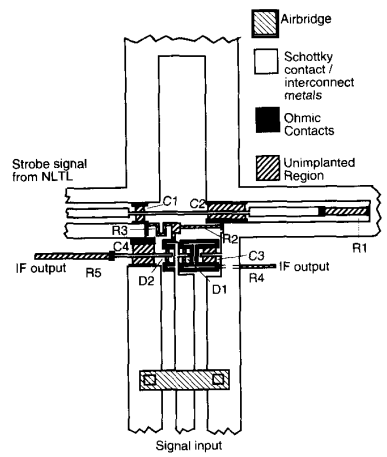

Fig. 3. Layout detail of the sampling circuit within the receiver IC.

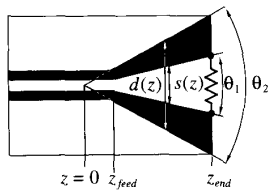

(a)

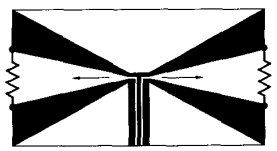

(b)

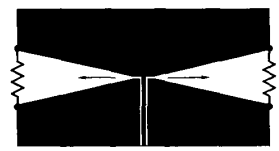

(c)

Fig. 4. The V (tapered CPS) antenna (A) and its dimensions. A pair of counterpropagating V antennas with a CPW feed (B) is similar to the bowtie antenna (C) in the limit $\theta_2 = 180°$. In all cases the traveling-wave antenna is terminated in its characteristic impedance.

Fig. 5 shows the skin loss determined from (1)–(3), while Fig. 6 shows the power radiated per unit distance $(2P_l(z)\alpha_r(z))$. Note, Fig. 6 has the position z_{peak} of peak radiation varies as $1/f$. Wider flare angles (θ_1,θ_2) increase the rate of radiation per unit distance, thereby decreasing skin-effect losses (Fig. 5). Increasing z_{feed} also decreases skin-effect losses, but we must set $z_{\text{feed}} < z_{\text{peak}}$ at the highest frequency of interest. The large angles of the bowtie antenna prevent use of the approximate analysis above, but we surmise that its large flare angles leads to losses at least as small as the 0.2 dB (at 1 THz) loss attainable on the CPS antenna.

III. The Measurement System

The measurement system is shown in Fig. 7. The transmitter and receiver IC's are placed on 16 mm diameter hyperhemispherical high-resistivity silicon substrate lenses. Planar antennas on dielectric substrates radiate primarily into the

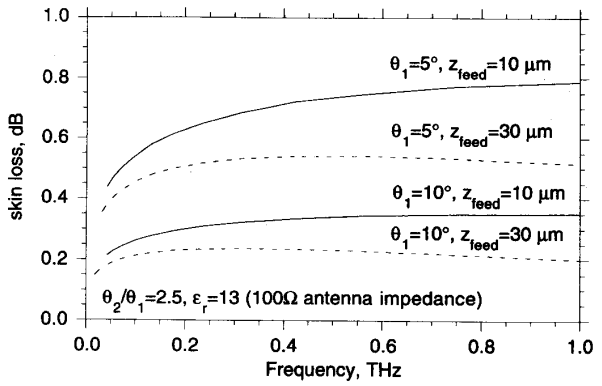

Fig. 5. Computed skin loss for $100\Omega V$ antennas on GaAs.

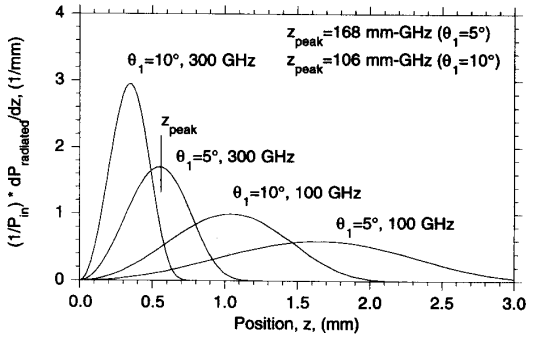

Fig. 6. Computed distribution of power radiated per unitdistance, normalized to the input power, on narrow-angle V antennas.

substrate [8]. The angle of total internal reflection is 16° from normal, and without the substrate lenses most of the radiated power would be reflected at the GaAs—air interface at the wafer back surface, resulting in low antenna efficiency. The substrate lenses permit the radiation to escape, and provide partial collimation. The radiated beam is collimated with off-axis parabolic mirrors (50 mm diameter, 33 mm focal length), and is focused on the receiver through similar optics. The transmitter NLTL is driven by a ~23 dBm sinewave at frequency f_{RF} = 7–14 GHz, generating a sawtooth waveform which is then radiated. The receiver NLTL is driven at $f_{LO} = f_{RF} - f_{IF}$, with typically f_{IF} = 100 Hz. At the receiver, the integrated NLTL-gated sampling circuit converts the received radio-frequency signal with repetition frequency f_{RF} to a sampled (intermediate-frequency) signal with repetition frequency f_{IF}. The sampled signal is observed on a digitizing oscilloscope. A mixer generates a phase reference signal for oscilloscope triggering, compensating for any phase drift between the two synthesizers. Two attenuators at oblique incidence on both sides of the sample under test suppress cavity resonances between the transmitter and receiver.

The lens system, bow-tie antennas, and their associated CPW baluns were characterized by a network analyzer connected to the antennas with microwave wafer probes (Fig. 8). With 7 mm antennas, a 10 GHz low-frequency cut-off is

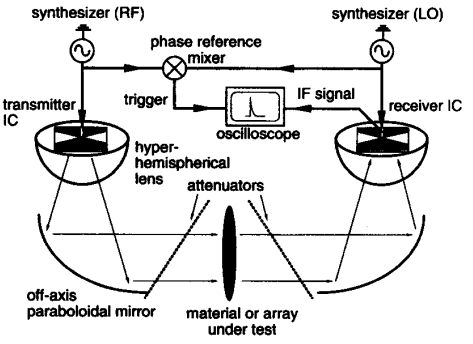

Fig. 7. Measurement system schematic diagram (left: transmitter, right: receiver). A mixer is used to generate a stable phase reference signal.

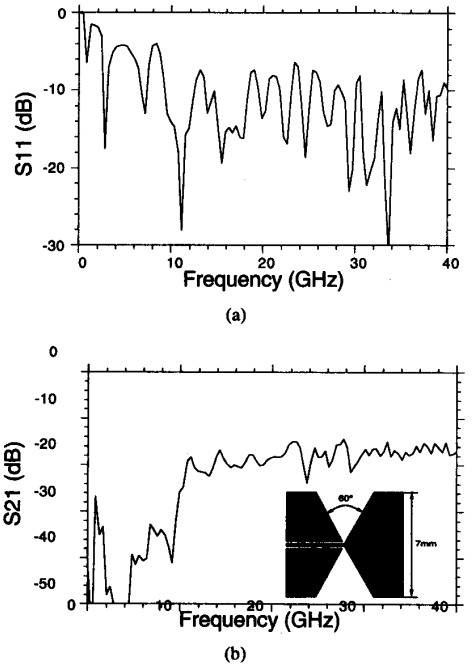

Fig. 8. Measured reflection coefficient (a) and system attenuation (b) for a pair of 7-mm bowtie antennas.

observed (Fig. 8). Simple ray-tracing arguments predict that the lenses will show spherical-mode resonances at multiples of 2.3 GHz (arising from reflections at the antenna-lens and lens-air interfaces); confirming this, the antenna return loss shows multiple resonances at ~2.6 GHz separation. With the hyperhemispherical lens, antenna radiation reflected from the lens-air interface reflects the antenna radiation towards a focal point below the antenna plane, and hence is defocused. Hyperhemispherical lenses therefore show weaker spherical resonances than hemispherical lenses. The insertion loss of the transmitter-receiver pair (Fig. 8 (b)) is 18.5 dB and is relatively flat from 10–40 GHz. Bow-tie antenna losses of 6 dB per antenna have been reported [12].

Several factors determine the antenna system bandwidth. The bow-tie antenna radiates efficiently only if its linear

dimensions are larger than a free space wavelength [8], giving the observed 10 GHz cut-off; a 2 mm length bow-tie exhibits a 35 GHz low-frequency cut-off. The substrate lens should also be several wavelengths diameter at the lowest frequency of interest. Diffraction also sets a low-frequency limit. With scale-invariant antennas, the collimated beam diameter w_0 emerging from the parabolic reflector is independent of wavelength. Under the approximation of a Gaussian beam [13] the $1/e$ beam radius $w(z) = w_0(1 + z^2/z_0^2)^{1/2}$ increases for propagation distances z greater than the waist length $z_0 = \pi w_0^2/\lambda$. With a reflector separation d, wavelengths much longer than $\lambda_c \simeq \pi w_0^2/d$ will have beam diameters substantially larger than the receiver's aperture, and the transmission efficiency drops. System bandwidth depends critically upon alignment. Scale-invariant antennas have effective aperture areas proportional to λ^2. Consequently, misalignment selectively attenuates high-frequency components in the received pulse train, limiting the system bandwidth.

IV. Control of Spurious Reflections

Although feasible, the current measurement system does not measure all four scattering parameters of the device under test. Because of this, full two-port calibration methods cannot be applied, and accurate transmission measurements (S_{21}) can be made only if the reflection coefficients of the source (transmitter) and detector (receiver) are small. While the calibration methods used here are similar to those used in microwave network measurements [14], [15], they differ from those used in experiments with laser-excited photoconductors [2].

The signal incident on the receiver should be only that passing through the sample. Some fraction of the radiated power will escape the collimated beam because of antenna sidelobes, Fresnel reflections at the lens-air interfaces, beam diffraction (at lower frequencies), and any off-normal reflection or scattering from the device under test. To control these spurious responses, metal surfaces surrounding the experimental apparatus are covered with microwave absorber (ferrite-filled rubber) to suppress spurious reflections. The experimental sample is mounted in an aperture in an absorber-covered wall placed between the transmitter and receiver.

Imaging the transmitter antenna onto the receiver produces a resonant cavity because of reflections (55% electric field reflection coefficient) at the air-lens interfaces. Because the incident radiation is not normal to the hyperhemispherical lens surface, the reflections are not fully collimated after passing back through the paraboloidal mirrors, and the apparent reflection coefficients of the transmitter and receiver hyperhemispherical lenses are reduced because of this defocusing. If we analyze the system consisting of the transmitter, the receiver, their respective reflection coefficients Γ_T and Γ_R, and the sample under test (described by s-parameters S_{ij}), then the received signal during the reference measurement has Fourier transform:

$$R_{\text{ref}}(\omega) = \frac{H_T(\omega)H_R(\omega)e^{-j\omega(l_1+l_2)/c}}{(1-e^{-2j\omega l_1/c}\Gamma_T)(1-e^{-2j\omega l_2/c}\Gamma_R) - e^{-2j\omega(l_1+l_2)/c}\Gamma_T\Gamma_R} \tag{4}$$

where $H_T(\omega)$ is the Fourier transform of the transmitted pulse, $H_R(\omega)$ is the Fourier transform of the receiver's impulse response, and l_1 and l_2 are the distances between the transmitter and the sample and the receiver and the sample. The received signal while measuring the device under test has a Fourier transform (5), shown at the bottom of the page: The measured transmission, the ratio of these two measurements, is (6), shown at the bottom of the pagewhich is accurate (close to S_{21}) only if Γ_T and Γ_R are made small.

To obtain accurate network measurements, transmitter and receiver reflections are suppressing by placing 5 dB thin-film metal attenuators at oblique incidence on both sides of the sample under test. Without these attenuators, transmission measurement errors of approximately ± 1 dB are seen in measurements similar to those of Fig. 13. The calibration method above provides a first-order correction arising to errors from misalignment between the transmitter and receiver, as the misalignment is present both during calibration and during measurement of the device under test. However, the device under test may deflect, focus, or defocus the transmitted signal, changing the system alignment and hence the measured transmission. A lens, for example, placed as the device under test between the transmitter and receiver, will defocus the propagating beam, reducing the received signal relative to that measured during calibration; the system would measure an attenuation resulting from the defocusing. Such effects are inherent to a free-space measurement system.

V. Bandwidth and Sensitivity

Given suppression of the cavity resonances or other spurious signals, the system accuracy, dynamic range, and usable bandwidth, is determined by the signal-to-noise ratio as a function of frequency.

Fig. 9 shows the received signal and Fig. 10 its power spectra with both the transmitter and receiver using 2 mm

$$R_{\text{meas}}(\omega) = \frac{H_T(\omega)H_R(\omega)S_{21}e^{-j\omega(l_1+l_2)/c}}{(1-e^{-2j\omega l_1/c}S_{11}\Gamma_T)(1-e^{-2j\omega l_2/c}S_{22}\Gamma_R) - e^{-2j\omega(l_1+l_2)/c}S_{21}S_{12}\Gamma_T\Gamma_R} \tag{5}$$

$$S_{21,\text{meas}}(\omega) = \frac{S_{21}\left((1-e^{-2j\omega l_1/c}\Gamma_T)(1-e^{-2j\omega l_2/c}\Gamma_R) - e^{-2j\omega(l_1+l_2)/c}\Gamma_T\Gamma_R\right)}{(1-e^{-2j\omega l_1/c}S_{11}\Gamma_T)(1-e^{-2j\omega l_2/c}S_{22}\Gamma_R) - e^{-2j\omega(l_1+l_2)/c}S_{21}S_{12}\Gamma_T\Gamma_R} \tag{6}$$

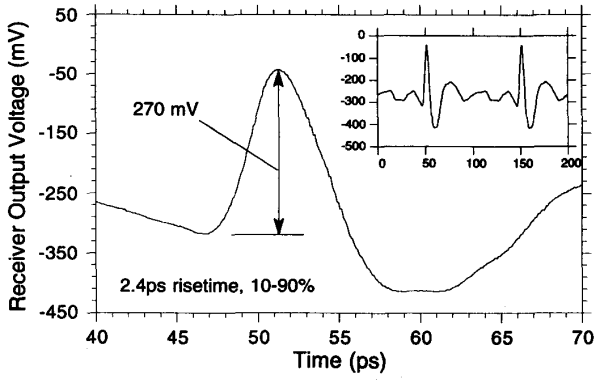

Fig. 9. Received waveform, without attenuators, at the sampling circuit output. The transmitter and receiver use 2 mm bow-tie antennas. In the inset the full period of the signal isshown.

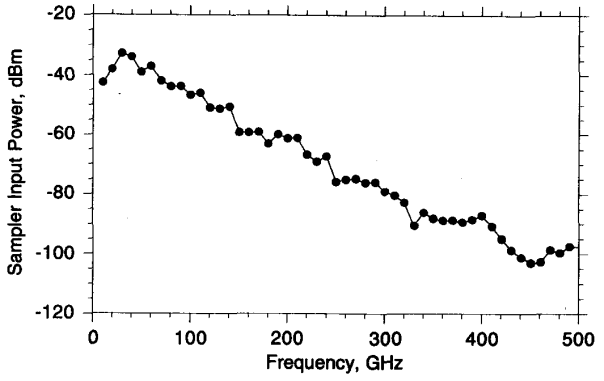

Fig. 10. Received power spectrum (with attenuators) at sampling circuit input, using 2 mm transmitter and receiver antennas.

square bow-tie antennas. The received waveform differs in form from the sawtooth waveform generated by the NLTL because of the antenna system 30 GHz low-frequency cutoff. As we will subsequently calculate and experimentally determine the sampling circuit noise figure (e.g. the input-referred noise power spectral density normalized to kT), the power spectrum of Fig. 10 is given in terms of the power at the *input* of the sampling circuit. The pulse has 2.4 ps risetime and 270 mV amplitude.

In the experimental configuration of Fig. 7, the two significant noise sources are the relative phase fluctuations (phase noise) of the two microwave synthesizers, and the receiver system noise, the latter being high because of the high sampling circuit noise figure and conversion loss. Phase noise is dominant. Although the two synthesizers share a common 10 MHz frequency standard, they have significant relative phase fluctuations. We can ascribe (without loss of generality) these timing fluctuations to the transmitter's (RF) synthesizer. Given zero phase noise, the received signal at the sampling circuit input will be $r(t) = r(t - n2\pi/\omega_{\mathrm{RF}})$, some periodic waveform with repetition frequency ω_{RF} . With phase noise, the RF synthesizer output is $V_0 \cos(\omega_{\mathrm{RF}}(t - J(t)))$, where $J(t)$ is the randomly- varying timing, $S_J(\omega) =$

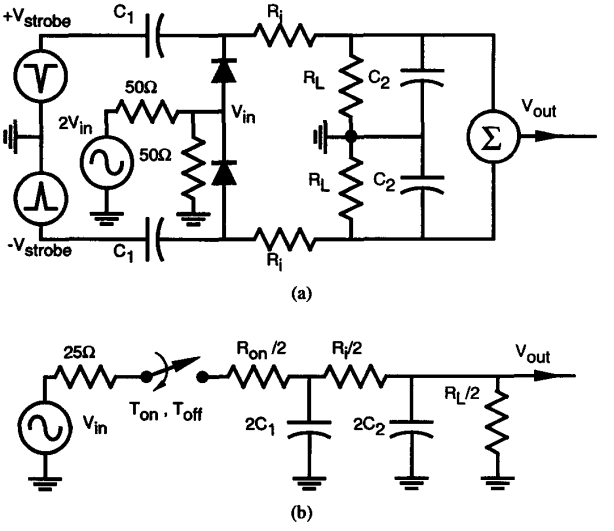

Fig. 11. Equivalent circuits of the sampling circuit (above), and reduced, equivalent single-channel circuit

$\int_{-\infty}^{+\infty} \langle J(t)J(t+\tau)\rangle e^{-j\omega\tau} d\tau$ its power spectral density, and the single-sideband phase noise spectral density of the RF synthesizer is $\mathcal{L}(\omega) = \omega_{\mathrm{RF}}^2 S_J(\omega)$. The sampling circuit input signal is now $r(t - J(t))$, and the power spectral density of $r(t)$ can be written as

$$S_R(\omega) = \sum_{n=0}^{+\infty} R_n \left(\delta(\omega - n\omega_{\mathrm{RF}}) + n^2\omega_{\mathrm{RF}}^2 S_J(\omega - n\omega_{\mathrm{RF}})\right) \quad (7)$$

This assumes $n\omega_{\mathrm{RF}}\sigma_J \ll 1$, where σ_J is the standard deviation of $J(t)$; R_n is the received power in the n^{th} harmonic of ω_{RF} (Fig. 10). Note that $J(t)$ has produced phase noise sidebands $n^2\omega_{\mathrm{RF}}^2 S_J(\omega - n\omega_{\mathrm{RF}})$ about each harmonic of ω_{RF}.

The receiver sampled (IF) output is the product $i(t) = r(t)s(t)$, where $s(t)$ is a sampling impulse train at repetition frequency $\omega_{\mathrm{LO}} = \omega_{\mathrm{RF}} - \omega_{\mathrm{IF}}$. The power spectrum of the sampled signal is

$$S_I(\omega) = G_s \sum_{n=0}^{+\infty} R_n \left(\delta(\omega - n\omega_{\mathrm{IF}}) + n^2\omega_{\mathrm{RF}}^2 S_J(\omega - n\omega_{\mathrm{IF}})\right), \quad (8)$$

plus terms at higher frequencies ($2\omega_{\mathrm{RF}}$, $2\omega_{\mathrm{LO}}$, $\omega_{\mathrm{RF}} + \omega_{\mathrm{LO}}$, etc.) which are removed by filtering. G_s is the sampling circuit conversion power gain (or loss). The measurement system determines the (vector) amplitude at frequency $n\omega_{\mathrm{RF}}$ of $r(t)$ by measuring the amplitude at frequency $n\omega_{\mathrm{IF}}$ of $i(t)$. Because $i(t)$ is downconverted to a low scan rate ω_{IF} (100 Hz), a given Fourier component of the pulse train are detected against a noise background set by the collective phase modulation sidebands of all other Fourier components. The signal/phase-noise ratio at $n\omega_{\mathrm{RF}}$ is

$$\frac{P_s}{P_{\text{phase noise}}} = \frac{R_n}{\left(\sum_{m=-\infty}^{m=+\infty} R_m m^2 \omega_{\mathrm{RF}}^2 S_J\left((n-m)\omega_{\mathrm{IF}}\right)\right)B}. \quad (9)$$

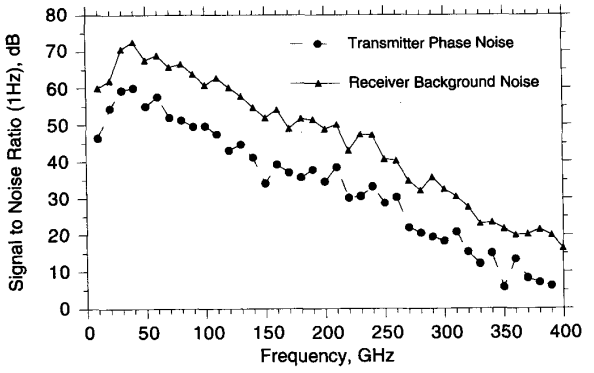

Fig. 12. Measured signal to phase noise and background noise ratios (with attenuators)

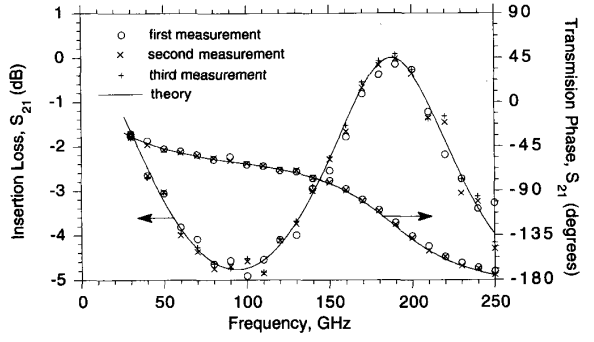

Fig. 13. Vector transmission measurement of a 254 μm thickness alumina test sample. left: insertion loss and right: phase.

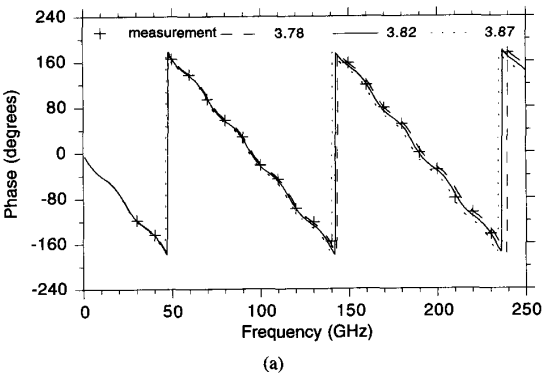

(a)

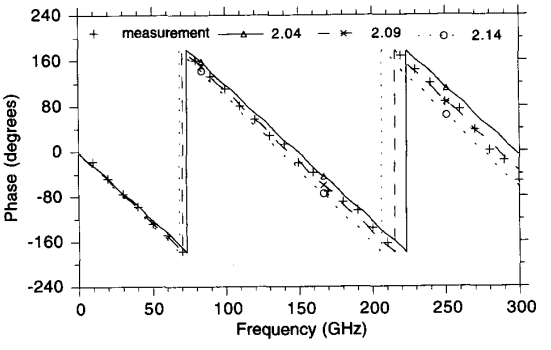

(b)

Fig. 14. Phase transmission measurement of (a) a 5080 μm thickness quartz test sample, (b) 4707 μm thickness Teflon test sample.The solid lines are theoretical fits with the indicated dielectric constants.

B is the bandwidth of the signal-processing subsequent to the receiver.

The receiver background (thermal) noise is much lower. Fig. (11(a)) shows an equivalent circuit for the sampling circuit. The circuit is balanced (symmetric), and a simpler single-channel equivalent circuit (Fig. 11(b)) is used for noise analysis. This model includes the 25 Ω source impedance, the isolation resistance $R_i = 1$ kΩ, the coupling capacitance $C_1 \simeq 20$ fF, the capacitance $C_2 \simeq 100$ pF of the cable connecting the receiver to the low-noise preamplifier, and the sampling diode on resistance $R_{\text{on}} = R_s + kT/qI_{\text{pulse}} \cdot R_s = 9\Omega$ is the diode parasitic series resistance, and I_{pulse} is the (average) strobe-pulse conduction current passing through the sampling diodes. The diodes' junction impedance $R_j = kT/qI_{\text{pulse}}$ has an associated short-circuit shot-noise current with spectral density $2qI_{\text{pulse}}$ (A^2/Hz), and hence R_j has an available noise power of $kT/2$ (W/Hz). For brevity, we will (pessimistically) assume an available noise power of kT (W/Hz) for R_j, the available noise power of a physical resistor. T_{on} is the sampling aperture time duration, and $T_{\text{on}} + T_{\text{off}} = 2\pi/\omega_{\text{LO}}$.

Sampling circuit analysis is similar to that applied to switched-capacitor filters [16]. Define the sampling duty cycle $D = T_{\text{on}}/(T_{\text{on}} + T_{\text{off}})$. If $[((50\ \Omega + R_{\text{on}})/D) \| R_i]C_1 \gg 1/\omega_{\text{LO}}$, then

$$\frac{V_{\text{out}}}{V_{\text{in}}} = \frac{R_L}{R_L + R_I + (50\ \Omega + R_{\text{on}})/D}, \tag{10}$$

the sampling circuit *operating* power gain is

$$\frac{P_{\text{out}}}{P_{\text{available}}} = 2\frac{50\ \Omega \cdot R_L}{[R_L + R_i + (R_{\text{on}} + 50\ \Omega)/D]^2}, \tag{11}$$

and the sampling circuit noise figure is

$$F = 2\frac{[R_i + (R_{\text{on}} + 50\ \Omega)/D][R_L + R_i + (R_{\text{on}} + 50\ \Omega)/D]}{50\ \Omega \cdot R_L}. \tag{12}$$

Most parameters in (12) are known device parameters, while the DC current at the sampling circuit IF port can be measured and is equal to $I_{\text{pulse}}D$. A 32 dB sampling circuit noise figure, and a -40.5 dB power gain are then calculated, given $R_L = 1$ MΩ. Comparing the measured signal/noise ratio (Fig. 12) to the measured received power spectrum (Fig. 10 (b)), the *measured* noise figure is $\sim 65 \pm 5$ dB, considerably larger than the predicted 32 dB.

VI. Measurements

Before using the system for measurements, its accuracy must be verified. Fig. 13 shows the amplitude (left) and the phase transmission measurements (right) of a 254 μm thin

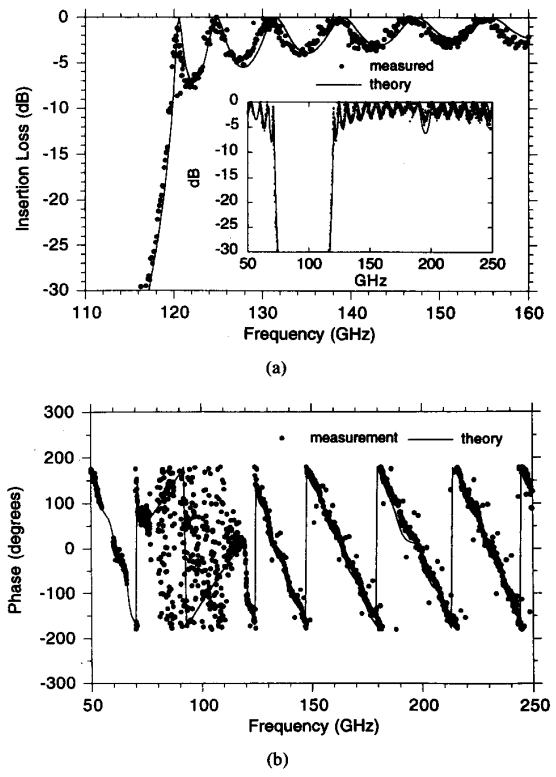

Fig. 15. Transmission measurement of a Bragg filter consisting of alternating layers of 10 pieces of alumina and 9 pieces ofTeflon. (a) insertion loss in 10–150 GHz and 100–300 GHz inset,illustrating the system frequency resolution. (b) phase transmission.

alumina substrate ($\epsilon_r = 9.9$). The measurement corresponds well to theory from 30 to 250 GHz with three subsequent measurements, with typical errors of ~0.2–0.4 dB. Commercial microwave network analyzers operating in the 45 MHz to 60 GHz range have accuracies of ~ 0.05 dB. Commercial network analyzers also use sampling circuits for signal detection downconversion and hence have similar receiver noise figures to the system reported here. The use of a pulsed stimulus signal with low IF frequencies in the system reported here introduces the effect of cumulative and overlapping phase-noise sidebands (c.f. Section V), a limitation which would be avoided if the stimulus signal had only a single Fourier component, as in commercial network analyzers. To some extent, the poorer accuracy of the reported system arises from difficulties inherent with free-space systems (e.g. alignment, spurious beam paths) and higher-frequency measurements (phase noise degradation during harmonic multiplication).

As a first application, the system was used to determine the dielectric constant of samples of fused quartz and Teflon. In Fig. 14(a), the measured phase transmission function of a 5.08 mm quartz sample was compared to calculation, and the dielectric constant adjusted in the calculation to obtain the best fit. The dielectric constant is determined as 3.82 ± 0.05. In Fig. 14(b), the measured phase transmission function of a 4.71 mm Teflon sample was also compared to calculation. The dielectric constant is determined as 2.09 ± 0.05.

Fig. 15 shows measurements of Bragg filter consisting of alternating layers of 10 pieces of alumina (254 μm thickness) and 9 pieces of Teflon (508 μm thickness). The measurement is noise-limited between 75 to 115 GHz. The filter shows 12 dB/GHz slope at 120 GHz.

VII. Conclusion

We have demonstrated a NLTL-based system for broadband mm-wave electromagnetic measurements. Reproducible, accurate measurements are possible from 30 to 250 GHz. The current system will allow convenient and accurate measurements of materials and mm-wave quasi-optical amplifier arrays. With improvements in NLTL and sampling circuit bandwidth (which we have recently obtained), combined with lower-phase-noise sources, system bandwidth can be significantly extended.

VIII. Acknowledgment

The authors are grateful for extensive discussions with David Rutledge, Robert York, Gabriel Riebez, and Richard Compton.

References

[1] "An 8-1000 GHz vector network analyzer," *Microwave Journal,* vol. 35, Mar. 1992.
[2] N. Katzenellenbogen and D. R. Grischkowsky, "Efficient generation of 380 fs pulses of THz radiation by ultrafast laser pulse excitation of a biased metal- semiconductor interface," *Appl. Phys. Lett.,* vol. 58, no. 3, pp. 222–224, January, 1991.
[3] Y. Konishi, M. Kamegawa, M. Case, R. Yu, M. J. W. Rodwell, *et al.*"Picosecond spectroscopy using monolithic GaAs circuits," *App. Phys. Lett.,* Vol. 61, No. 23, pp. 2829–2831, December 1992.
[4] M. J. W. Rodwell, C. J. Madden, B. T. Khuri-Yakub, D. M. Bloom, Y. C. Pao, *et al.*, "Generation of 7.8 ps electrical transients on a monolithic nonlinear transmission line," *Electron. Lett.,* vol. 24, no. 2, p. 100, Jan. 21, 1988.
[5] M. J. W. Rodwell, M. Kamegawa, R. Yu, M. Case, E. Carmen, *et al.*, "GaAs nonlinear transmission lines for picosecond pulse generation and millimeter-wave sampling," *IEEE Trans. Microwave Theory Tech.,* vol. 39, pp. 1194–1204, July 1991.
[6] R. A. Marsland, C. J. Maden, D. W. Van Der Weide, M. S. Shakouri, and D. M. Bloom, "Monolithic integrated circuits for mm-wave instrumentation," in *Tech. Dig., GaAs IC Symp.,* New Orleans, LA. Oct. 7–10, 1990.
[7] V. H. Rumsey, *Frequency-Independent Antennas.* New York: Academic, 1966.
[8] D. B. Rutledge, D. P. Neikirk, and D. P. Kasilingam, "Integrated-circuit antennas" in K. J. Button, Ed.,*Infrared and Millimeter Waves,* Vol. 10. New York: Academic Press, 1984, pp. 1–90.
[9] R. C. Compton, R. C. McPhedran, Z. P. Popovic, G. M. Rebeiz, P. P. Tong *et al.*, "Bow-tie antennas on a dielectric half-space: Theory and experiment," *IEEE Trans. Antenna Propag.,* AP-35, pp. 622–631, June 1987.
[10] A. Moussessian and D. B. Rutledge, "A millimeter-wave slot-V antenna," *IEEE AP-S Int. Symp.,* Chicago, IL, July 18–25, 1992.
[11] R. Hoffmann, *Handbook of Microwave Integrated Circuits.*Norwood, MA: Artech House, 1987.
[12] D. B. Rutledge and M. S. Muha, "Imaging antenna arrays," *IEEE Trans. Antenna Propag.,* AP-30, no. 4, July 1982.
[13] S. Ramo, J. R. Whinnery, and T. VanDuzer, *Fields and Waves in Communication Electronics.* New York: Wiley, 1984.
[14] D. Rytting, "Advances in microwave error correction techniques," Hewlett-Packard, RF & MW Symp., 1987.
[15] D. R. Gagnon, " Highly sensitive measurements with a lens-focused reflectometer," *IEEE Trans. Microwave Theory Tech.,* vol. 39, Dec. 1991.
[16] R. Unbehaven and A. Cichocki, *MOS Switched-Capacitor and Continuous-Time Integrated Circuits and Systems* New York:. Springer-Verlag, 1985.

Yoshiyuki Konishi was born February 16, 1965, in Hyogo, Japan. He received the B.S. and M.S. degrees in applied physics from Osaka University, Japan, in 1987 and 1989, respectively.

In 1989, he joined Shimadzu Corporation, Kyoto, Japan, where he developed high voltage generator for accelerator, which is used for high energy ion beam analysis. He worked as a visiting scientist at the University of California, Santa Barbara from 1991 to 1993, and engaged in research on application of nonlinear transmission lines for mm-wave spectroscopy and on development of Schottky-collector resonant tunneling diode. He is currently working in research and development of high energy ion beam analysis and implantation at Shimadzu Corporation, Keihanna Laboratories, Kyoto, Japan.

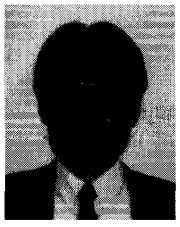

Masayuki Kamegawa was born September 27, 1958, in Shiga, Japan. He received the B.S. and M.S. degrees in applied physics from Osaka University, Osaka, Japan, in 1982 and 1984, respectively.

In 1984, he joined Shimadzu Corporation, Kyoto, Japan, where he developed semiconductor X-ray detector for medical imaging systems. He worked as a Visiting Scientist at the University of California, Santa Barbara from 1989 to 1991, and engaged in research on application of nonlinear transmission lines and high speed samplers. He is currently working in research and development of semiconductor lasers and application at Shimadzu Corporation, Keihanna Laboratories, Kyoto, Japan.

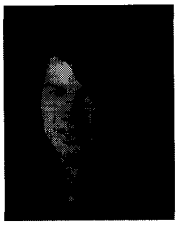

Michael Case received the B.S., M.S., and Ph.D,. degrees in electrical engineering from the University of California, Santa Barbara, in 1989, 1991, and 1993, respectively.

He is currently a member of the technical staff at Hughes Research Laboratories, Malibu, CA.

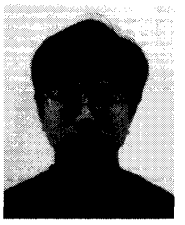

Ruai Yu received the B.S. degree in electrical engineering from San Francisco State University, San Francisco, CA and the M.S. degree in electrical engineering from the University of California, Santa Barbara, in 1988 and 1991, respectively. He is currently a Ph.D. candidate at the latter university.

From 1988 to 1989, he was with Ampex Corporation developing advanced equalization techniques for high-speed digital recording channels. His research interests are the design and fabrication of high speed devices and integrated circuits, and the development of millimeter-wave instrumentation.

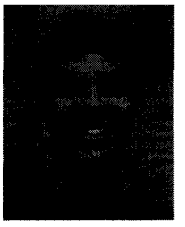

Scott T. Allen received the B.S. degree in electrical engineering from Cornell University, Ithaca, NY, and the M.S. degree from the University of Massachusetts, Amherst, in 1987 and 1989, respectively. He is currently pursuing the Ph.D. degree at the University of California, Santa Barbara.

From 1987 to 1990, he worked at the Martin Marietta Electronics Laboratory, where he was involved with HEMT characterization and the design of mm-wave circuits. His current research is in the area of sub-mm wave electronics.

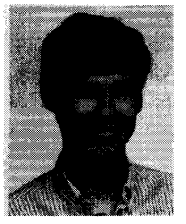

Mark J. W. Rodwell received the B.S. degree in electrical engineering from the University of Tennessee, Knoxville, the M.S. and Ph.D. degrees from Stanford University, Stanford, CA, in 1980, 1982, and 1988, respectively.

From 1982 to 1984, he worked at AT&T Bell Laboratories, developing optical transmission systems. In 1988, he was a Research Associate at Stanford University. Currently, he is an Associate Professor in the Department of Electrical and Computer Engineering, University of California, Santa Barbara. His current research involves picosecond electrical shock-wave and soliton devices, millimeter-wave generation and instrumentation, picosecond optoelectronic devices, optical probing of electronics, resonant tunneling diodes, and millimeter wave HBT and HEMT circuit design.

Dr. Rodwell is the recipient of a 1989 National Science Foundation Presidential Young Investigator Award.